

Accepted Manuscript

Tumor microenvironment-targeted poly-L-glutamic acid-based combination conjugate for enhanced triple negative breast cancer treatment

Juan J. Arroyo-Crespo, Ana Armiñán, David Charbonnier, Leandro Balzano-Nogueira, Francisco Huertas-López, Cristina Martí, Sonia Tarazona, Jerónimo Forteza, Ana Conesa, María J. Vicent

PII: S0142-9612(18)30660-4

DOI: [10.1016/j.biomaterials.2018.09.023](https://doi.org/10.1016/j.biomaterials.2018.09.023)

Reference: JBMT 18894

To appear in: *Biomaterials*

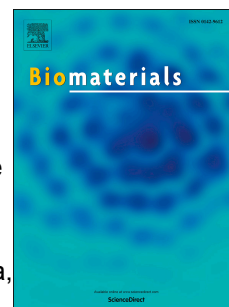
Received Date: 6 June 2018

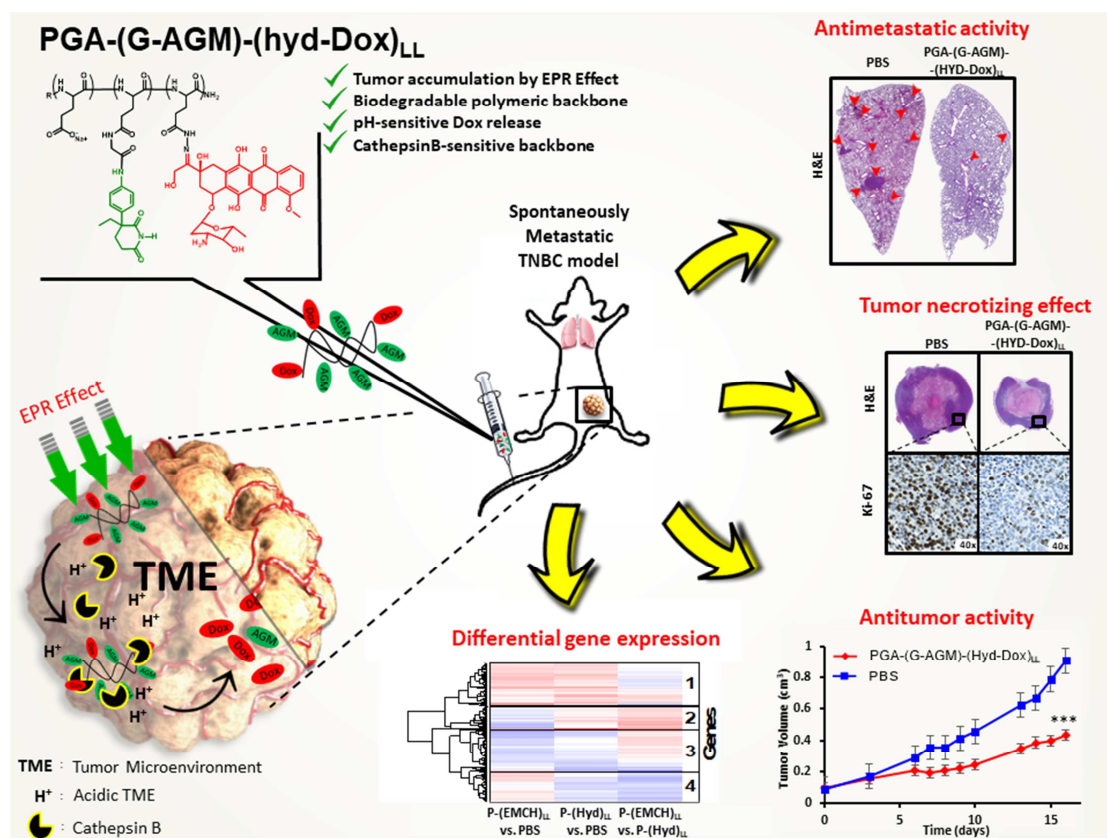
Revised Date: 11 September 2018

Accepted Date: 14 September 2018

Please cite this article as: Arroyo-Crespo JJ, Armiñán A, Charbonnier D, Balzano-Nogueira L, Huertas-López F, Martí C, Tarazona S, Forteza Jeró, Conesa A, Vicent MaríJ, Tumor microenvironment-targeted poly-L-glutamic acid-based combination conjugate for enhanced triple negative breast cancer treatment, *Biomaterials* (2018), doi: <https://doi.org/10.1016/j.biomaterials.2018.09.023>.

This is a PDF file of an unedited manuscript that has been accepted for publication. As a service to our customers we are providing this early version of the manuscript. The manuscript will undergo copyediting, typesetting, and review of the resulting proof before it is published in its final form. Please note that during the production process errors may be discovered which could affect the content, and all legal disclaimers that apply to the journal pertain.





Tumor Microenvironment-Targeted poly-L-glutamic acid-based Combination Conjugate for Enhanced Triple Negative Breast Cancer Treatment

Juan J. Arroyo-Crespo¹, Ana Armiñán^{1}, David Charbonnier^{1,2}, Leandro Balzano-Nogueira³, Francisco Huertas-López³, Cristina Martí⁴, Sonia Tarazona⁴, Jerónimo Forteza⁵, Ana Conesa^{3,4}, María J. Vicent^{1,2*}*

¹Polymer Therapeutics Laboratory, Centro de Investigación Príncipe Felipe, Av. Eduardo Primo Yúfera 3, Valencia 46012, Spain.

²Screening Platform, Centro de Investigación Príncipe Felipe, Av. Eduardo Primo Yúfera 3, Valencia 46012, Spain.

³Microbiology and Cell Science Department, Institute for Food and Agricultural Sciences, Genetics Institute, University of Florida, Gainesville, USA

⁴Genomics and Gene Expression Laboratory, Centro de Investigación Príncipe Felipe, Av. Eduardo Primo Yúfera 3, Valencia 46012, Spain.

⁵Unidad Mixta CIPF-IVP Centro de Investigación Príncipe Felipe, Av. Eduardo Primo Yúfera 3, Valencia 46012, Spain.

* Address Correspondence to: aarminan@cipf.es or mjvicent@cipf.es

Keywords

Polymer therapeutics, polypeptides, tumor microenvironment, polymer-based combination conjugates, metastatic triple-negative breast cancer, transcriptomics

ABSTRACT

The intrinsic characteristics of the tumor microenvironment (TME), including acidic pH and overexpression of hydrolytic enzymes, offer an exciting opportunity for the rational design of TME- drug delivery systems (DDS). We developed and characterized a pH-responsive biodegradable poly-L-glutamic acid (PGA)-based combination conjugate family with the aim of optimizing anticancer effects. We obtained combination conjugates bearing Doxorubicin (Dox) and aminoglutethimide (AGM) with two Dox loadings and two different hydrazone pH-sensitive linkers that promote the specific release of Dox from the polymeric backbone within the TME. Low Dox loading coupled with a short hydrazone linker yielded optimal effects on primary tumor growth, lung metastasis (~90% reduction), and toxicological profile in a preclinical metastatic triple-negative breast cancer (TNBC) murine model. The use of transcriptomic analysis helped us to identify the molecular mechanisms responsible for such results including a differential immunomodulation and cell death pathways among the conjugates. This data highlights the advantages of targeting the TME, the therapeutic value of polymer-based combination approaches, and the utility of -omics-based analysis to accelerate anticancer DDS.

1. Introduction

The hypoxic and acidic environment of the tumor microenvironment (TME) promotes the survival of cancer cells over normal cells [1] and represents a crucial target for the newest generation of anticancer drug delivery systems (DDS). The higher glycolytic rate of tumor cells generates and sustains the acidic character of the TME [2] and provides a rationale for the specific design of targeted DDS. If properly engineered, nanoscale therapeutics passively accumulate within the TME of adequately vascularized tumors [3-5] by the enhanced permeability and retention (EPR) effect and the presence of pH-labile linkers within the DDS can trigger conjugated drug release. Other than TME-targeting of pH-labile DDS, endocytic internalization promotes lysosomal degradation [6] of polymers such as poly-L-glutamic acid (PGA), thanks to the presence of hydrolytic enzymes such as Cathepsin B [7] as well as an acidic pH.

Our laboratory recently reported the development of PGA-based combination conjugates bearing a synergistic ratio of the anthracycline drug doxorubicin (Dox) and the aromatase inhibitor Aminoglutethimide (AGM) [8]. Specific engineering of the three-dimensional (3D) conformation permitted similar optimal release rates for Dox and AGM, with release rate representing the parameter controlling drug-drug synergism [8, 9], translating to enhanced antitumor efficacy in an orthotopic 4T1 triple negative breast cancer (TNBC) preclinical model [10]. The release of both drugs via protease-cleavable drug linkers relied on the heterogeneous expression of various hydrolytic enzymes within the TME activity (at both the patient [11] and tumor level [12]). This fact highlights the need for patient stratification in DDS treatment cohorts, a requirement exemplified by clinical data obtained for Opaxio®, which displayed optimal activity in phase III clinical trials in premenopausal women with optimally high levels of estrogen to promote cathepsin B activity [13].

We aimed to potentiate the therapeutic capacity of our previously described PGA-combination conjugates by further promoting metastasis inhibition through the incorporation of a pH-labile linker for Dox (simple hydrazone moiety or complex EMCH [N- ϵ -maleimidocaproic acid hydrazide] moiety), while retaining the optimized glycine-based linking chemistry for AGM [8], using our metastatic TNBC mice as preclinical model [10]. Of note, TME-targeting represents a promising alternative means to inhibit metastasis in

TNBC, a particularly aggressive breast cancer subtype that features a unique microenvironment distinct from that of other subtypes, especially when compared to Luminal A [14, 15]. Furthermore, as a consequence of molecular complexity and heterogeneity, TNBC lacks the targeted treatments available for other subtypes.

During this study, we discovered that low Dox loading and shorter hydrazone linkers yielded optimal antitumor and antimetastatic effects in our TNBC model. RNA sequencing (RNA-seq) analysis employed to explore the mechanism of action of TME-targeted conjugates revealed the inhibition of metastatic pathways and the importance of immunomodulation. This powerful genomics tool allowed us to elucidate the functional aspects of gene expression driving cell death at the genome-wide level and the establishment of relationships with the physico-chemical descriptors. As far as our knowledge, this is one of the few experimental analysis of this type within Polymer Therapeutics and demonstrates the enormous potential of polymer genomics [16] to elucidate molecular mechanism of action and identify promising molecular targets.

2. Materials and Methods

Detailed materials and ethical statements can be found in Supplementary Information (SI).

2.1. Synthesis of Polymer-drug Conjugates

2.1.1. Synthesis of Single Conjugates

Detailed synthetic procedure for single conjugates can be found in Supplementary Information (SI)

2.1.2. Synthesis of combination conjugates

2.1.2.1. Synthesis of PGA-(G-AGM)-Hyd-Dox

We employed an optimized protocol derived from a previously described strategy by Van Heeswijk in order to generate PGA-Hyd-Dox conjugates [17]. Hydrazone-based combination conjugates were synthesized by one-pot direct attachment of G-AGM and tert-butyl-carbazate. Further Boc deprotection of the amino-group allowed final Dox coupling. PGA (300 mg, 2.32 mmol, 1.0 eq., 100 units, Mw ~13 KDa) was dissolved in 10 ml of anhydrous DMF in an inert atmosphere. DMTMM.BF₄ (0.3 eq.) was added to the solution and 15 min later G-AGM (0.164 mmol, 58.2 mg) and tert-butyl-carbazate (18.38 mg, 0.139 mmol, 0.06 eq. for 5% modification) were added. The reaction proceeded for 48 h and the workup was performed as already described procedure for the workup of PGA-NH-NHBoc (see SI). Once the stability of G-AGM in TFA was ensured (**Fig. SI5**), Boc release was performed as for the synthesis of PGA-NH-NH₂ (see section 2.3.1.2) and Dox was coupled through a hydrazone bond following the same procedure as for the synthesis of PGA-hyd-Dox (see SI).

2.1.2.2. Synthesis of PGA-(G-AGM)-EMCH-Dox

EMCH-Dox-based combination conjugates were synthesized by one-pot direct attachment of G-AGM and PD and further EMCH-Dox coupling through the reduction of PD. PGA (300mg, 2.32 mmol, 1.0 eq., 100 units, Mw~13 KDa) was dissolved in 10 ml of anhydrous DMF in an inert atmosphere. DMTMM.BF₄ (i.e. 15.34 mg, 0.116 mmol, 0.05 eq. for 5% modification) was added to the solution and 15 min later G-AGM (0.164 mmol, 58.2 mg) and PD (30.9 mg, 0.139 mmol, 0.06 eq. for 5% modification) were added. The reaction proceeded for 48 h and the workup was performed as for the PGA-NH-NHBoc. An aliquot was isolated

for G-AGM and PD loading determination. For EMCH-Dox attachment, PGA-(G-AGM)-PD was dissolved in anhydrous DMF and EMCH-Dox (750.76 g/mol, 1.5 eq. with respect to PD modification) was dissolved and TCEP (0.15 eq. with respect to the PD modification) was finally added as reducing agent. Boc release was performed as for the synthesis of PGA-NH-NH₂ (see **SI**) and Dox was coupled through a hydrazone bond following the same procedure as for the synthesis of PGA-hyd-Dox (see **SI**).

To note, detailed Physico-chemical Characterization protocols can be found in **SI**.

2.2. Cell Culture and *In vitro* Cytotoxicity Analysis of Conjugate

The 4T1 cell line was maintained in RPMI supplemented with 10% heat inactivated FBS at 37°C in a controlled atmosphere of air / CO₂ (95/5 vol./vol.). Media was replaced every 48 - 72 hours and underwent passaging when 80% cell confluence was reached. Cytotoxic assays were performed according to a previously described protocol [8]. In brief, cells were seeded in sterile 96-well microtiter plates at concentration of 6,250 cells/cm². Further details can be found in **SI**.

2.3. Drug Release kinetics

2.3.1. pH-dependent Drug Release

Specific Dox release under mild acidic conditions was demonstrated *in vitro* by liquid-liquid extraction and further quantification by reversed-phase high-performance liquid chromatography (RP-HPLC). The conjugates were incubated in 50 mM PBS at pH 7.4 and pH 5.0, mimicking the blood and tumor (and/or lysosomal) environment respectively. See **SI** for detailed information.

2.3.2. Cathepsin B-dependent Drug Release Kinetics

Cathepsin B (5 U) was added to a solution of 2 mg of each conjugate, in 1 mL of a pH 6 buffer composed of 20 mM sodium acetate, 2 mM ethylenediaminetetraacetic acid (EDTA), and 5 mM dithiothreitol (DTT). The incubation was carried out at 37°C. Aliquots (100 µl) were taken at times up to 48 h, immediately frozen in liquid nitrogen, and stored in the dark until assayed by HPLC as described above for pH-dependent drug release assay. The free

drug (0.75 mg/mL) was also incubated under same conditions and later used as the reference control.

2.4. Evaluation of *in vivo* Antitumor Activity and Safety of Conjugates

2.4.1. Establishment of Highly Metastatic 4T1 murine Breast Cancer Model and *in vivo* Validation of Conjugates

The spontaneously metastatic TNBC model was developed as previously reported [8, 10]. See **SI** for further information

2.4.2 *In vivo* study at 10 mg/Kg Dox-equivalent dose

Eight days before induction, tumor sizes reached 0.1 cm³ and mice were split into representative groups. Conjugate-based treatments were dissolved in sterile PBS and immediately injected intravenously (i.v.) in four doses of 10 mg/Kg of Dox equivalents every three days (See **Fig. 4A** and **SI**).

2.4.3. Hematological Study

Blood was extracted immediately after sacrificing mice by cardiac puncture with a 1.0 ml heparinized syringe and transferred to a 2 ml Eppendorf tube. Blood was gently homogenized and left to reach RT and then kept at 4 °C until analysis (within the first 30 min after extraction). Serum was isolated by centrifugation (4000 rpm, 10 min, 4 °C) and analyzed using an automated hematologic analyzer (Sysmex XT-2000i).

2.4.4. Histopathological Study

All tissues were washed in fresh PBS, carefully dried, weighed, and fixed in paraformaldehyde (PFA) at room temperature for 24 h. PFA was eliminated by successive washing with PBS (5 times x 20 min, rapid agitation). Once washed, tissues were stored in a solution of PBS with 0.05% of sodium azide as preservative at 4 °C protected from light. Further conventional Hematoxylin-Eosin staining was carried out (see **SI** for further details).

2.4.5. Safety Evaluation of Treatments

Treatments safety was evaluated by tracking body weight and comparisons with control and healthy animals, as well as further histopathological studies of key organs. The mice under study were examined daily in the search for any pain-related behavior or conduct modification. Postmortem, major organs were also analyzed histopathologically for any treatment-derived damage.

2.4.6. Tumor Density

Tumor density was obtained by simple arithmetic calculation and allowed us to elucidate differential stromal arrangement due to the different treatments.

2.5. Evaluation of the Antimetastatic Effect of Conjugates in the Lung

Lung metastasis was evaluated following a previously described protocol [20] with several improvements. See **SI** for a detailed protocol.

2.6. Transcriptomic study

2.6.1. Extraction of RNA from Frozen Tumors and Sequencing

Total RNA isolation was performed from 50 mg of previously pulverized frozen tumor employing the PureLink RNA Mini kit (Ambion-Life Technologies) following manufacturer's recommendations. The On-column PureLink DNase Kit (Invitrogen) was used to purify the DNA-free RNA. The qualification and integrity of total RNA was performed with an Agilent Technologies 2100 Bioanalyzer (or 4200 Tape Station). TruSeq Stranded mRNA libraries were constructed and sequenced at Macrogen (Seoul, Korea) using an Illumina HiSeq4000 platform (paired-end with a length of 100 bp).

2.6.2. Mapping and Quantification

Raw paired-end sequences were mapped against the mouse reference genome with STAR aligner software [21]. There was no need to trim or filter due to the high quality of the samples, checked with FastQC tool (URL:

<https://www.bioinformatics.babraham.ac.uk/projects/fastqc/>). The mapping step was completed with a mean of an 88% of uniquely mapped reads. The quantification of the transcripts was performed with RSEM software [22].

2.6.3. RNA-seq Data Analysis

Low count genes in RNA-seq count data were filtered with NOISeq package [23] and kept for the statistical analysis the 14,323 genes having an average of more than one read count per million reads in any of the four experimental groups. The resulting count matrix was normalized by the sequencing depth to make samples comparable. Data were transformed with the Voom approach [24] to get a normal distribution. The limma R package [25], which is based on linear models, was used to obtain the differentially expressed genes among experimental groups. Further information on the different comparison established can be found in **SI**.

2.6.4. Functional Analysis

Gene Ontology functional enrichment analysis using the Fisher's exact test was performed for genes selected (nominal p-value <0.01) at each of the above comparisons. Additionally, the log2-fold change at each pair wise comparison was calculated and exported to PaintOmics 3 [27] for KEGG pathway analysis. KEGG pathways were manually edited to improve interpretation of functional analysis results.

3. RESULTS AND DISCUSSION

3.1. Synthesis and Characterization of Polymer-drug Conjugates

We previously demonstrated optimal therapeutic benefit with PGA-AGM-Dox combination conjugates presenting a differential (faster) Dox release rate when compared to AGM in an orthotopic TNBC model [10]. To further enhance this effect, we incorporated hydrazone-based pH-sensitive linkers for Dox conjugation while retaining the original optimized linking chemistry for AGM (Gly-AGM).

As shown in **Fig. 1A** and **Fig SI1**, we employed two different pH-sensitive hydrazone linkers: we used the direct conjugation through the C-13 Dox ketone [17] or conjugation employing a flexible, hydrophobic, and longer maleimido linker (EMCH) that we hypothesized would provide even faster Dox release. Direct conjugation required the previous modification of the PGA backbone with tert-butylcarbazate. The EMCH spacer required the previous modification of Dox to obtain EMCH-Dox as well as previous modification of the PGA backbone with a PD moiety. The last stage involved the reduction of the disulphide bond to yield the conjugate through the thioether derivative (**Fig. 1A, SI1**). This Dox-linker strategy has its origin in the development of Aldoxorubicin (formerly, INNO-206, EMCH-Dox) as a bovine serum albumin (BSA)-binding-Dox prodrug [28] and has been reported previously for a PGA-based combination conjugate [29].

Additionally, to explore the effect of different Dox loadings and encouraged by preliminary results demonstrating enhanced cytotoxicity in the lower Dox loading range [8], we fixed G-AGM content in all combination conjugates at 10% mol, but varied Dox loading from 1% mol (Low Loading [LL]) to 3% mol (High Loading [HL]) (**Fig. 1C**). Unfortunately, we could not generate the single conjugate incorporating a high loading of the bulky EMCH moiety (PGA-EMCH_{HL}), probably due to steric impediments. We performed the direct attachment of G-AGM and the precursor moieties (tert-butylcarbazate and PD) by carbodiimide coupling to achieve our combination (**Fig. 1A**) and single conjugates (**Fig. SI1**).

We then carried out physico-chemical characterization of all synthesized conjugates (see SI). **Fig. 2B** depicts the spectra of representative conjugates with chemical shifts attributed to the incorporation of one or both drugs. The signal corresponding to the ethylene group (δ 0.75 ppm) and those at the aromatic region (δ 7.5 ppm) indicated the presence of G-AGM. Dox aromatic rings signals appeared in the region of δ 7.0-8.0 ppm and the methylene group of the amino-sugar moiety at δ 1.25 ppm. The conjugates bearing EMCH-Dox, presented a characteristic ethylene signal of the EMCH spacer (δ 3.3 ppm) also present in the combination conjugate; however, the aromatic signals of the drug practically disappeared. Additionally, the broadening of polymer signals also represented a sign of polymer conjugation.

We also employed ^1H -NMR to evaluate single conjugates precursors, PGA-PD, PGA-NH-NHBoc, PGA-NH-NH₂, and the combination conjugates precursors PGA-(G-AGM)-PD,

PGA-(G-AGM)-NH-NHBoc, and PGA-(G-AGM)-NH-NH₂ (**Fig. SI3** and **SI4**). Additional ¹H-NMR assignments of final conjugates (**Fig. SI12**) can be compared with the corresponding spectra of the free parent drugs, demonstrating the presence of the drug within the nanoconjugate structure (**Fig. SI11**).

SEC elugrams demonstrated single homogeneous Mw distribution by refractive index (RI), and no evidence of free drug presence (**Fig. 2D, E**). We note that the conjugation of one or both drugs did not significantly modify the D_h in solution by DLS (number) and most of the conjugates exhibited a monomodal averaged D_h of ~3-6 nm, except in the case of the single conjugate PGA-(Hyd-Dox)_{LL} (D_h ~290 nm) and the combination conjugate PGA-(G-AGM)-(EMCH-Dox)_{LL} (D_h ~18 nm). Interestingly, DLS measurements in terms of intensity (**Fig. SI13**), revealed a bimodal population distribution indicating the coexistence of unimers and aggregates. Although we expected the higher Dox-loaded conjugates and those bearing the hydrophobic EMCH linker to markedly aggregate given the overall increased hydrophobicity, we actually observed greater aggregation behavior for those with the lowest Dox content. This counterintuitive finding may indicate that the overall aqueous solution conformation is driven by a complex interplay of dynamic factors (including the polyelectrolyte effect [30, 31]) and not only imposed by the hydrophobicity of the loaded drugs as a single factor [8]. We aim to undertake additional studies involving complementary techniques, such as in-flow fractionation techniques [30, 32] to reveal the contribution of both, hydrophobicity and polyelectrolyte effect to the global spatial arrangement of conjugated macromolecules.

3.2. Dox Release Kinetics as a Crucial Feature Driving *in vitro* Output

To understand the biological implications of different drug linker use and drug loading/ratio in our conjugates, we performed cell toxicity assays in 4T1 murine breast cancer cells. **Fig. 3A** depicts the *in vitro* effect of the PGA-(G-AGM)-(Hyd-Dox)_{HL}, PGA-(G-AGM)-(Hyd-Dox)_{LL}, PGA-(G-AGM)-(EMCH-Dox)_{HL}, and PGA-(G-AGM)-(EMCH-Dox)_{LL} combination conjugates. Cell viability assays demonstrated higher cytotoxicity for the PGA-(G-AGM)-(Hyd-Dox)_{LL}, PGA-(G-AGM)-(Hyd-Dox)_{HL}, and PGA-(G-AGM)-(EMCH-Dox)_{LL} combination conjugates when compared with PGA-(G-AGM)-(EMCH-Dox)_{HL}, which displayed very low cytotoxicity (**Fig. 3A**). Although cytotoxicity assays provided non-statistically-significant differences at the range of concentrations tested, both combination

conjugates incorporating low Dox loadings presented with trends towards higher cytotoxicity ($IC_{50} = 0.13 \mu\text{g/mL}$ and $0.45 \mu\text{g/mL}$ for $\text{PGA}-(\text{G-AGM})-(\text{EMCH-Dox})_{\text{LL}}$ and $\text{PGA}-(\text{G-AGM})-(\text{Hyd-Dox})_{\text{LL}}$, respectively, vs. $IC_{50}=0.79 \mu\text{g/mL}$ for $\text{PGA}-(\text{G-AGM})-(\text{Hyd-Dox})_{\text{HL}}$) (**Fig. 3B**). In contrast with our previously reported $\text{PGA}-(\text{G-AGM})$ -Dox family [8], we did not observe any significant differences in cell toxicity between the single and the combination conjugates (**Fig. SI15**), indicating a lack of AGM:Dox synergism at the drug ratios present upon hydrazone-mediated conjugation.

To explain this biological/therapeutic output, we evaluated Dox release from the combination conjugates at physiological and acidic pH as well as in the presence of Cathepsin B (**Fig 3C** and **Fig SI16**) and, as expected, we found differential release profiles depending on Dox loading and linker length. For the EMCH-derivatives, the $\text{PGA}-(\text{G-AGM})-(\text{EMCH-Dox})_{\text{LL}}$ combination conjugate displayed rapid Dox release at pH 5.0 during the first 8 h, reaching a maximum of 16%, and a slower Dox release ($\sim 2\%$) at physiological pH (7.4). Remarkably, the corresponding combination conjugate with higher Dox loading, $\text{PGA}-(\text{G-AGM})-(\text{EMCH-Dox})_{\text{HL}}$, displayed almost no Dox release at pH 5 or 7.4 ($<1\%$) during the same time period (**Fig SI16A-B**). These results, together with DLS measurements (by number) (**Fig. 2C**), suggest a distinct conjugate solution conformation, due to a different spatial arrangement of Dox molecules as a function of loading. We hypothesize that high loading of EMCH-Dox promotes a more condensed structure (lower D_h), with the hydrazone bond hidden from the acidic environment and thereby hindering Dox release. This may also explaining the difficulty we faced when attempting to increase Dox loading. Therefore, we also hypothesize that low loadings of EMCH-Dox correlate with a more swollen structure (higher D_h), promoting a higher level of hydrazone exposure and Dox release.

Conjugates obtained by direct conjugation displayed similar Dox loading-related release behavior (**Fig. 3C** and **Fig SI16C**). The $\text{PGA}-(\text{G-AGM})-(\text{Hyd-Dox})_{\text{LL}}$ combination conjugate exhibited up to 10% Dox released at pH 5.0 within 8 h and less than 1% at pH 7.4. In contrast, the $\text{PGA}-(\text{G-AGM})-(\text{Hyd-Dox})_{\text{HL}}$ combination conjugate displayed only 2% Dox release at pH 5.0 within the same time frame. Independently of the Dox linking chemistry employed, lower loading correlated higher release rates, thereby explaining the differential cytotoxicity observed. For hydrazone-derivative conjugates, we did not find any differences by DLS in terms of number. However, measurement by intensity suggested a higher aggregation tendency (larger D_h) for the combination conjugate bearing the lower Dox

loading (PGA-(G-AGM)-(Hyd-Dox)_{LL}) when compared to the corresponding conjugate with higher Dox loading (PGA-(G-AGM)-(Hyd-Dox)_{HL} (**Fig. 2C, Fig. SI13**).

As we conjugated AGM through a pH-stable chemical bond, we expect AGM release from the PGA mainchain by cathepsin B-driven degradation [8]. Therefore, we expected much faster overall Dox release rates from Dox-hydrazone-bearing conjugates than AGM release (only influenced by protease presence). However, cathepsin B degradation studies with (PGA-(G-AGM)-(Hyd-Dox)_{HL} (**Fig SI16C**) clearly show that this assumption was wrong and that the final conjugate solution conformation again was critical. The greater AGM bioavailability *vs.* Dox obtained for this conjugate, could be responsible for the lack of activity as well as drug synergism discovered. In the case of the most active conjugate, (PGA-(G-AGM)-(Hyd-Dox)_{LL} (**Fig 3C**), same results were seen, however in this particular case, and we believe is the reason for the enhanced activity, Dox release profile was faster at very early time-points (at pH 5 as well as in presence of cathepsin B, showing the preferential hydrolytic mechanism triggering Dox release). Also, the final relative release profile comparing Dox *vs* AGM could explain the absence of drug synergism as an inverse relative bioavailable AGM:Dox ratio from that previously identified as synergistic [8] was obtained.

In summary, the release kinetics findings fully correlate with *in vitro* results: the combination conjugate displaying the highest IC₅₀ (PGA-(G-AGM)-(EMCH-Dox)_{HL}) demonstrated almost no Dox release, while the conjugate showing the highest Dox release (PGA-(G-AGM)-(EMCH-Dox)_{LL}) corresponded to the highest cytotoxicity. As demonstrated previously [8, 33], the selection of drug linkers, drug ratios, and drug loadings in a polymer-drug combination conjugate can drastically modify the entire macromolecular configuration, varying key parameters, including hydrodynamic size and drug release kinetics, that directly influence biological readout.

3.3. Study of combination conjugates antitumor activity and safety in a spontaneously metastatic TNBC murine model

The antitumor/antimetastatic effect of polymer-drug combination conjugates requires accumulation within the tumor site by passive (EPR effect) accumulation and/or active targeting. We and others have previously described the spontaneously metastatic 4T1 TNBC

murine model developed in immunocompetent BALB/c mice [10, 34, 35], which included the study of EPR effect [4]. This preclinical model faithfully mimics the human clinical scenario, offering an opportunity for reliable DDS *in vivo* testing [10].

To examine combination conjugate antitumor efficacy, we randomly distributed tumor-bearing mice whose volumes had reached $\sim 0.1 \text{ cm}^3$ (maximal EPR effect [10]) into representative groups and scheduled four treatments every three days with the conjugates showing the best cytotoxic activity (at 10 mg/kg Dox equivalents) (**Fig. 4A**). In addition, we administered Dox to a control group at 5 mg/kg and unconjugated PGA as a vehicle control at 25 mg/kg (maximum concentration used for the conjugates as carrier). Both PGA-(G-AGM)-(Hyd-Dox)_{LL} and PGA-(G-AGM)-(EMCH-Dox)_{LL} combination conjugates exhibited substantial antitumor activity (50% tumor reduction compared with PBS-treated mice) (**Fig. 4B**). Furthermore, we noted a similar decrease in tumor volume in the free Dox-treated animals. However, treatment with unconjugated PGA and PGA-(G-AGM)-(Hyd-Dox)_{HL} did not significantly diminish tumor growth when compared with PBS-treated mice. In good agreement with our *in vitro* findings we did not find improvement on efficacy when we administered the physical mixture of single conjugates (PGA-(G-AGM) + PGA-(Hyd-Dox)_{LL}) or the combination conjugate PGA-(G-AGM)-(Hyd-Dox)_{LL} in comparison to the administration of the PGA-(Hyd-Dox)_{LL} single conjugate, suggesting, in this case, that the presence of AGM does play a relatively minor role (**Fig SI14**). As stated above, this result could be explained by the differential bioavailable drug ratio achieved when compared to previous protease labile PGA-AGM-Dox conjugates [8] (**Fig. 3C and SI16**). Dox concentration in the tumor site is significantly higher at early time points and more importantly it relies on a hydrolytic trigger, therefore, we would expect Dox released already in the tumor stroma, but not AGM (**Fig 3C**).

To further understand the effect of our combination conjugates on tumor growth, we studied tumor density (**Fig. 4C**) and the relationship between proliferation (via Ki-67 immunostaining of axial sections) and tumor necrosis (**Fig. 4D**) at the experimental endpoint. We did not see significant tumor necrosis within the free Dox treated animals, perhaps due to lower levels of persistence within the tumor stroma (**Fig. 4D**). However, treatment with the two combination conjugates displaying the most promising therapeutic effects (PGA-(G-AGM)-(Hyd-Dox)_{LL} and PGA-(G-AGM)-(EMCH-Dox)_{LL}) led to the appearance of large necrotic tumor cores (**Fig. 4D**) and optimal tumor growth inhibition (**Fig. 4B**). Furthermore,

these two combination conjugates inhibited the proliferation of outer viable cells (**Fig. 4D**), indicating possible cell-cycle arrest induced by prolonged Dox exposure driven by both passive conjugate accumulation and sustained stromal release [36, 37]. Although necrosis is typically related with hypodense tissue regions, our analyses demonstrated higher necrosis in the denser tumors ($\sim 1.9 \text{ g/cm}^3$ vs. placebo $\sim 1.4 \text{ g/cm}^3$) (**Fig. 4D**). PGA-(G-AGM)-(Hyd-Dox)_{HL} treated tumors presented the lowest density, similar to the PBS control group ($\sim 1.3 \text{ g/cm}^3$) (**Fig. 4D**). Of note, 4T1 tumors develop coagulative necrosis [38, 39] characterized by the preservation of the basic structural outline of the affected cells in a compact network and the accumulation of inflammatory cells [40]. Dox-related hypoxia [41] may lead to tumor tissue ischemia and thus to more hypoxic tumors resulting in increased coagulative necrosis and therefore, denser tumors. Additionally, we found evidence of calcification in the core of the densest tumors (PGA-(G-AGM)-(EMCH-Dox)_{LL}), which corresponds to the rapid fast development of necrosis, in response to a highly effective antitumor treatment. Such calcification could drastically increase tumor weight and, therefore, tumor density.

To assess safety, we systematically evaluated, body weight, general aspect, behavior, and post-mortem major organ weights of all animals employed. We observed no significant alterations in body weight of animals treated with PGA-(G-AGM)-(Hyd-Dox)_{LL}, PGA-(G-AGM)-(Hyd-Dox)_{HL}, or Dox, which displayed a 100% survival rate (**Fig. 4E** and **F**). However, PGA-(G-AGM)-(EMCH-Dox)_{LL} treated presented with lethargy, weakness, and slight dyspnea immediately following the third and fourth iv. administrations, with only 50% of animals surviving (**Fig. 4F**). Post-mortem organ analysis revealed increased relative liver weight in all animals compared to healthy (non-tumor bearing animals) noting the largest relative liver weight increase in animals treated with PGA-(G-AGM)-(EMCH-Dox)_{LL} (**Fig. 4G**). However, we note that animals treated with PGA-(G-AGM)-(Hyd-Dox)_{LL}, PGA-(G-AGM)-(Hyd-Dox)_{HL}, and Dox exhibited smaller increases in relative liver weight when compared to the PBS-treated (tumor-bearing) control animals, suggesting better overall anti-tumor activity (see below for further details).

Of the organs studied, histopathological analyses revealed treatment-related adverse effects in the liver, as noted, and the heart, one of the key organs that present anthracycline-related pathologies [42, 43]. The liver presented significant hydropic degeneration, suggesting possible treatment-associated toxicity (**Fig. SI17**) and hearts of animals treated with Dox presented with myocardial fiber tortuosity, interfibrillar edema, and abundant

fibrosis as major cardiomyopathies (**Fig. 4H**). Although we discovered some disperse regions presenting minor levels of fibrosis, we observed no other major Dox-related cardiomyopathies in animals treated with two most effective antitumor treatments (PGA-(G-AGM)-(EMCH-Dox)_{LL} or PGA-(G-AGM)-(Hyd-Dox)_{LL}).

All combination conjugates demonstrated safer *in vivo* therapeutic characteristics in terms of body weight and cardiotoxicity compared to free Dox (at even half dosage). Nevertheless, the PGA-(G-AGM)-(EMCH-Dox)_{LL} combination conjugate-treated animals demonstrated low overall survival and some degree of hepatotoxicity. Of note, the PGA-(G-AGM)-(EMCH-Dox)_{LL} combination conjugate exhibited the lowest Dox loading (**Fig. 2A**), and so, we required highly concentrated doses of the conjugate to reach desired Dox equivalents, which increased the final solution viscosity; a parameter with the potential to affect proper blood distribution. Second, the larger size and heightened ability of this combination conjugate to aggregate in solution (**Fig. 2C**) might promote accumulation in other organs, as well as in the tumor. Livers from animals receiving PGA-(G-AGM)-(EMCH-Dox)_{LL}, developed even higher hydropic degeneration (vacuolar degeneration), coinciding with organ swelling (**Fig. 4H**), when compared with free Dox treatment [42] (**Fig. SI17**). Chemotherapeutic drug-induced hydropic degeneration occurs by direct and indirect toxicity mechanisms. The direct action causes increased cell membrane injury [44] leading to cellular injury (e.g. antineoplastic drugs such as cisplatin and Dox). The indirect action includes the release of highly toxic and reactive free radicals [45] causing lipid peroxidation and cell membrane damage [46] with increased influx of sodium and water causing cellular swelling. Therefore, enhanced liver toxicity and reduced overall survival might be the result of a sum of factors, such as the possible accumulation of this conjugate and corresponding Dox-associated toxicity in liver.

Overall, the PGA-(G-AGM)-(Hyd-Dox)_{LL} combination conjugate displayed the best antitumor activity and the greatest inhibition of tumor cell proliferation without impairing safety, thereby demonstrating the benefits of the rationally designed polymer conjugation-based strategies.

3.4. Study of Antimetastatic Activity of Combination Conjugates and Effects over Extramedullary Hematopoiesis and Leukemoid Reaction

Lung metastasis is the most common complication in breast cancer patients and is identified in 60-70% of all cancer patients [47]. During primary tumor progression, cancer cells can escape from the tumor stroma and travel through the bloodstream or lymphatic system, generating metastatic foci within the lung parenchyma or in the subpleural region. The 4T1 orthotopic TNBC BALB/c murine model is suitable for antimetastatic nanomedicines validation as it faithfully mimics the human clinical scenario, including spontaneously metastatic to the lung [10, 34]. This model develops the first signs of lung metastasis around day 3 after cells implantation although our scheduled treatment began at day 8 (max EPR). As depicted in **Fig. 5A**, the PGA-(G-AGM)-(hyd-Dox)_{LL} combination conjugate displayed optimal antimetastatic activity: a 90% reduction in lung metastasis when compared with non-treated mice. The EMCH-based conjugate incorporating the lowest Dox loading (PGA-(G-AGM)-(EMCH-Dox)_{LL}) displayed the same antimetastatic potential as free Dox. Further histopathological analysis confirmed these results (**Fig. 5B**); animal receiving PGA-(G-AGM)-(hyd-Dox)_{LL} treatment (optimal antitumor combination conjugate) also displayed reduced subpleural and intraparenchymatous metastatic foci when compared with other treatments.

4T1 tumor development blocks medullar erythropoiesis and, as a consequence, causes splenic and hepatic erythropoiesis, which promotes acute splenomegaly in mice [10, 48, 49]. We evaluated the capacity of combination conjugates to reduce this secondary effect of tumor progression by examining spleen weights and histopathological features. As depicted in **Fig. 5C**, we observed significant decreases in spleen weight in mice treated with PGA-(G-AGM)-(Hyd-Dox)_{LL}, PGA-(G-AGM)-(EMCH-Dox)_{LL}, or free Dox (the most effective antitumor treatments), with spleen weight in the PGA-(G-AGM)-(Hyd-Dox)_{HL} treated animals similar to PBS (tumor-bearing) animals. Further histopathological analyses confirmed previous findings (**Fig. 5D**). We discovered severe congestion of the red pulp and hyperplasia due to elevated reactive hematopoiesis in the spleens of PBS control mice and the combination conjugate PGA-(G-AGM)-(EMCH-Dox)_{HL} treated mice (**Fig. 5D**). Spleens from mice treated with Dox, PGA-(G-AGM)-(Hyd-Dox)_{LL}, or PGA-(G-AGM)-(EMCH-Dox)_{LL} displayed a partially restored splenic parenchyma. However, the severe leukemoid (leukocytosis) reaction observed in the PBS treated mice developed to a lesser extent in animals treated with Dox or

with PGA-(G-AGM)-(Hyd-Dox)_{LL} (**Fig. 5E-G**), in line with the slower overall disease progression.

The reduction in metastasis at the experimental endpoint might imply two different antimetastatic mechanisms induced by our combination conjugates. Greater anti-tumor activity (primary tumor), a reduction of tumor growth and tumor-cell proliferation, may also inhibit metastatic-related processes, including angiogenesis, migration, and/or epithelial-mesenchymal transition of tumor cells. Additionally, given the enhanced size in solution of the conjugates, the higher ability to aggregate, and the accelerated Dox release kinetics of the low loading combination conjugates could promote accumulation in the lungs [50], leading to a direct effect on metastatic tumor cells. We hope that additional experiments focused on lung accumulation will corroborate these hypotheses.

In summary, the combination conjugates with lower Dox loading exhibit higher antitumor and antimetastatic activity, coinciding with higher Dox release influence by the conjugate solution conformation and tumor stromal features.

3.5. Transcriptomic study of Combination Conjugates

3.5.1 GO Analysis

To understand the molecular basis of the responses to the different combination conjugates, we performed RNA-seq analysis of tumors derived from treated animals and compared genes differentially regulated between each possible pair-wise comparison (**Fig. SI18**). In agreement with the above-described physiological characterization assays, we found that the highest number of differentially expressed genes, compared to the PBS control group, corresponded to the PGA-(G-AGM)-(Hyd-Dox)_{LL} and PGA-(G-AGM)-(EMCH-Dox)_{LL} combination conjugates, while the PGA-(G-AGM)-(Hyd-Dox)_{HL} combination conjugate that shows no differences in tumor growth inhibition with respect to PBS control had significantly lower numbers of differentially expressed genes. We therefore concentrated our functional enrichment analysis on PGA-(G-AGM)-(Hyd-Dox)_{LL}, and PGA-(G-AGM)-(EMCH-Dox)_{LL} treatments to understand similarities and differences between molecular responses.

GO enrichment analysis revealed the enrichment of 62 and 5 terms in genes that were up- or down-regulated, respectively, when comparing (PGA-(G-AGM)-(Hyd-Dox)_{LL} and PGA-(G-

AGM)-(EMCH-Dox)_{LL}) transcriptional responses (**Fig. 6A**), while 11 and 10 GO terms were enriched in up- or down-regulated genes between the two conjugates.

Upregulated processes common for PGA-(G-AGM)-(Hyd-Dox)_{LL} and PGA-(G-AGM)-(EMCH-Dox)_{LL} include chemotaxis, positive regulation of interferon gamma-mediated (IFN- γ) signaling pathway, response to interferon alpha (IFN- α), granzyme-mediated apoptotic signaling pathway, and autophagy of host cells, amongst others (**Fig. 6B**), indicating that treatment induced a shared activation signature related to inflammation, apoptosis induction and autophagy activation.

Interferon signaling pathways (IFN- α and IFN- γ) are involved in immune response, inhibition of cell proliferation, inflammation, immune surveillance and tumor suppression by inducing the transcription of a number of IFN-stimulated genes [51]. Binding of IFN- γ and IFN- α to their respective receptors promotes the activation of PI3K/AKT and JAK/STAT pathways [51, 52], resulting in the synthesis of several pro-apoptotic factors, but also inhibiting the synthesis of anti-apoptotic genes [53]. Accordingly, we detected the upregulation of the granzyme-mediated pathway, a process that involves T-cell mediated cytotoxicity and perforin-granzyme-dependent killing of the cell through the induction of apoptosis [54], found in our enrichment results. Moreover, we detected upregulation of autophagy, which is a different type of active programmed cell death [55]. Interestingly, both treatments caused a marked upregulation of T-cell chemotaxis; T-cell trafficking to and increasing the T-cell frequency at the TME is one of the major challenges for adoptive immunotherapy as a new strategy against tumor development and metastasis [56].

Taken together these upregulated pathways indicate the contribution of different cell death mechanisms, including processes leading to apoptosis and others mediating autophagy, in both PGA-(G-AGM)-(Hyd-Dox)_{LL} and PGA-(G-AGM)-(EMCH-Dox)_{LL} treatments.

Both treatments also provoke the downregulation of processes related to cell proliferation, signaling and metastasis, blood vessel development (angiogenesis), epithelial-mesenchymal transition (EMT), epithelial cell proliferation involved in mammary gland duct elongation, and positive regulation of protein kinase C (**Fig. 6C**).

The link between angiogenesis and EMT is widely accepted, since the same factors that drive endothelial cells toward a pro-angiogenic phenotype may also drive epithelial cells toward a mesenchymal stem cell (MSC) phenotype. Thus, angiogenesis can be accomplished through

endothelial sprouting or non-sprouting microvascular growth, in a similar manner that endothelial cells gain invasive and migratory properties to become MSCs [57]. In this context, EMT and angiogenesis have emerged as integral processes in the promotion of carcinogenesis [58, 59].

Moreover, genes related to epithelial cell proliferation involved in mammary gland duct elongation also displayed a downregulation. This GO term includes different genes, all of them playing an important role in mammary gland organogenesis and development [60]. The mammary gland epithelium passes through several cycles of proliferation and cell death during pregnancy, lactation, and involution. However, many of the signaling mechanisms that control the initial invasion of the fat pad by the epithelium and regulate its continuing plasticity can be harnessed or corrupted by tumor cells in order to support their aberrant growth and progression towards invasion [61]. Accordingly, we hypothesize that at least part of the anti-cancer activity of our conjugates might be mediated by the inhibition in the proliferation of mammary gland cells

Additionally, the PGA-(G-AGM)-(Hyd-Dox)_{LL} and PGA-(G-AGM)-(EMCH-Dox)_{LL} combination conjugates downregulate the protein kinase C (PKC) pathway, which could imply deactivation of NF κ B signaling [62]. Overexpression of the factor NF- κ B is frequently found in cancer and other inflammatory diseases and a potential inhibition of NF- κ B here could be an additional anticancer effect of our combinatorial therapy.

As mentioned, we discovered a total of 67 GO terms (5 downregulated terms and 62 upregulated terms) enriched in a comparison between PGA-(G-AGM)-(Hyd-Dox)_{LL} and PGA-(G-AGM)-(EMCH-Dox)_{LL} treated tumors. This indicates a stronger and more general effect of PGA-(G-AGM)-(Hyd-Dox)_{LL} when treating tumor cells compared to PGA-(G-AGM)-(EMCH-Dox)_{LL}. PGA-(G-AGM)-(EMCH-Dox)_{LL} involves fewer targeted processes, such as stem cell proliferation and epidermal cell differentiation, indicating a role of this combination conjugate in reducing cancer cell growth (**Fig. 6D**). PGA-(G-AGM)-(Hyd-Dox)_{LL} specifically activates general processes such as defense/immune responses, inflammation, phagocytosis, cell signaling and metastasis (**Fig. 6E**), suggesting that the PGA-(G-AGM)-(Hyd-Dox)_{LL} is more effective in provoking a general immune response that might contribute to fight tumor progression, improve health status of the individual and increase survival rates. In this sense, we observed higher survival rates of mice treated with PGA-(G-AGM)-(Hyd-Dox)_{LL}, which corroborates this assumption.

3.5.2 Pathway Analysis Highlights Mechanistic Differences between PGA-(G-AGM)-(Hyd-Dox)_{LL} and PGA-(G-AGM)-(EMCH-Dox)_{LL}

We used the PaintOmics 3 tool to create a mechanistic representation of some of the processes involved in the PGA-(G-AGM)-(Hyd-Dox)_{LL} and PGA-(G-AGM)-(EMCH-Dox)_{LL} modes of action. PaintOmics 3 analysis confirmed and expanded GO enrichment results in relation to cell survival/apoptosis (**Fig. 7A**) and inflammation, angiogenesis, and metastasis (**Fig. 7B**), revealing additional similarities and differences between the two conjugates.

We uncovered evidence of both conjugates inducing apoptosis through the activation of the granzyme (GZMB) signaling pathway (**Fig. 6B**). Indeed, we found strong upregulation of GZMB and perforin (PRF1) for both treatments (**Fig. 7A**, see first two columns of gene heatmaps); however, we also detected activation of the apoptosis extrinsic pathway (**Fig. 7A**), which involves the activation of cell surface death receptors (FAS, TNFR) by extracellular ligands such as FAS-L or TNF, resulting in the cleavage or activation of caspase-8 and a signaling cascade that culminates in cell death [63]. We note the strong upregulating of all these markers for both conjugates (**Fig. 7A**)

We demonstrate the differences between the two conjugates in the third column of the gene heatmaps (**Fig. 7A**). PGA-(G-AGM)-(Hyd-Dox)_{LL} exhibits consistent activation of typical pro-apoptotic markers such as tubulin alpha 1b (TUBA1B), poly(ADP-Ribose) polymerase 1 (PARP1), beta-actin (ACTB), and myeloid cell leukemia sequence 1 (MCL1) (red in gene heatmaps). However, PGA-(G-AGM)-(EMCH-Dox)_{LL} more frequently triggers the overexpression of cell survival and anti-apoptotic genes, including as B-cell lymphoma 2 (BCL2), growth arrest and DNA damage inducible alpha (GADD45A), baculoviral IAP repeat containing 2 (BIRC2), mouse double minute 2 homolog (MDM2), and TNF receptor associated factor 1 (TRAF1) (blue in gene heatmaps). From these observations, we hypothesize that PGA-(G-AGM)-(Hyd-Dox)_{LL} treatment is not only stronger in provoking apoptosis through upregulation of proapoptotic processes, but also reduces the expression of genes related to cell survival and anti-apoptosis, jointly contributing to a strong apoptotic response.

Pathway enrichment analysis also revealed stronger angiogenesis and inflammation activities for PGA-(G-AGM)-(Hyd-Dox)_{LL} treatment than for PGA-(G-AGM)-(EMCH-Dox)_{LL} (**Fig. 6D**). Prostaglandin-endoperoxide synthase 2 (PTGS2), a marker of pro-angiogenesis processes [64] that, although overexpressed for both conjugates, exhibited higher levels for PGA-(G-AGM)-(Hyd-Dox)_{LL} treatment (**Fig. 7B**). Similarly, although inflammation was a hallmark of both treatments (**Fig. 6B**), selected inflammatory biomarkers such as Interleukin (IL)1B, IL6, Interferon- γ and TNF- α were upregulated following PGA-(G-AGM)-(Hyd-Dox)_{LL} treatment compared to PGA-(G-AGM)-(EMCH-Dox)_{LL} (**Fig. 7B**), which might mediate the differential inflammatory response between the two conjugates.

Protein tyrosine kinase 2 (PTK2) and the matrix metalloproteinases 1 and 9 (MMP1 and MMP9) displayed higher levels in PGA-(G-AGM)-(EMCH-Dox)_{LL} treatment (**Fig. 7B**), suggesting that these genes might mediate the increased trend for heightened metastatic activity observed in PGA-(G-AGM)-(EMCH-Dox)_{LL} treated tumors when compared to PGA-(G-AGM)-(Hyd-Dox)_{LL}.

4. Conclusions

Both experimental results and transcriptional analysis indicate that the two most effective conjugates, PGA-(G-AGM)-(Hyd-Dox)_{LL} and PGA-(G-AGM)-(EMCH-Dox)_{LL}, target the TME to trigger a cascade of molecular events that promote tumor cell death (apoptosis and autophagy) and inhibit tumor-related activities, including metastasis and cell proliferation.

However, we also highlight significant differences between the two combination conjugates: PGA-(G-AGM)-(Hyd-Dox)_{LL} triggers a more intense immune response that might explain why recipient mice display a higher survival rate. Also, PGA-(G-AGM)-(Hyd-Dox)_{LL} leads to higher pro-apoptotic activity, lower anti-apoptotic signals, and inhibition of metastasis, which support the overall response to this treatment.

We have also demonstrated the relative importance of targeting the TME for drug release and optimizing the bioavailable drug ratio in a combination therapy, highlighting the importance of a chemical rational for polymer-drug(s) linker design. Adequate drug release kinetics represents a crucial parameter towards achieving an adequate safety: efficacy ratio and may secure an adequate therapeutic window for future treatments.

Finally, this study also demonstrates the utility of side-by-side transcriptional analysis that serves to understand our results and promote the future design of advanced polymer-based DDS for the treatment of metastatic TNBC among others.

FIGURE LEGENDS

Fig. 1. Synthetic scheme followed to achieve for Poly-L-glutamate (PGA)-based combination conjugates. **i. a)** DMTMM.BF₄, DIEA, anh-DMF, 15min, R.T. **i. b)** t-butyl carbazate, G-AGM, 24h, pH=8, R.T.; **ii)** TFA, 30min, R.T.; **iii. a)** DOX.HCL, CH₃COOH (cat.), 36h. **iii. b)** NaHCO₃ (dil) **iv. a)** DMTMM.BF₄, DIEA, anh-DMF, 15min, R.T. **iv. b)** Pyridyldithiol, G-AGM, 24h, pH=8, R.T.; **v. a)** EMCH-Dox, TCEP (cat.); **v. b)** NaHCO₃ (dil).

Fig. 2. Physicochemical characterization of PGA-based combination conjugates. **A)** Physico-chemical characteristics of PGA-drug conjugates. **B)** Representative ¹H-NMR spectra (D₂O, 300 MHz). **C)** Size distribution graphs in number obtained by DLS in PBS at 5.0 mg mL⁻¹. **D)** and **E)** SEC chromatograms for parental PGA compared with single conjugates and combination conjugates, respectively (RI detection, peak at 17.1 corresponds to the counter-cation Na⁺)

Fig. 3. Cell viability and kinetics of drug release studies for combination conjugates. **A)** Cell viability measured by MTS assay after 72 hours of treatment with PGA-(G-AGM)-(Hyd-Dox)_{LL}, PGA-(G-AGM)-(Hyd-Dox)_{HL}, PGA-(G-AGM)-(EMCH-Dox)_L, PGA-(G-AGM)-(Hyd-Dox)_{HL} or free Dox. Data expressed as mean ± SEM, at least n = 3 experiments per treatment. **B)** Determination of IC₅₀ for the free Dox and the polymer-drug conjugates in mouse 4T1 breast cancer cell line. **C)** Kinetics of drug(s) release from PGA-(G-AGM)-(Hyd-Dox)_{LL} under hydrolytic as well as proteolytic (cathepsin B) conditions; n = 3 experiments per assay.

Fig. 4. In vivo antitumor and safety evaluation of combination conjugates in an orthotopic TNBC mice model. **A)** Routine schedule of treatment administration. The treatment started at the previously determined Max EPR point. **B)** Tumor growth inhibition of previously selected polymer-drug conjugates. Data represents mean ± SEM. Statistical significance was determined using an ANOVA t-test, (* p<0.05, ** p<0.01, *** p<0.001). **C)** Mice weight loss along treatments **D)** Comparison of tumor density with different treatments

at the experimental endpoint. **E)** Comparison of H&E and Ki-67 axial sections of tumors at experimental endpoint after different treatments. **F)** Mice-treated heart sections showing Dox-induced cardiotoxicity by means of H&E and Masson's immunostaining compared with the cardio-safety displayed by the combination conjugates. **G)** Kaplan-Meyer survival curves demonstrating safety of the combination conjugates with the exception of PGA-(G-AGM)-(EMCH-Dox)_{LL}, that shows only 50% of mice survival. **H)** Relative liver weight by treatments demonstrating tumor-related hepatomegaly in the PBS group, that partially was improved with Dox, PGA-(G-AGM)-(Hyd-Dox)_{HL}, PGA-(G-AGM)-(Hyd-Dox)_{LL} and greater organ weight related to the treatment PGA-(G-AGM)-(EMCH-Dox)_{LL}. Statistical significance was determined using an ANOVA t-test (* $p < 0.05$, ** $p < 0.01$, *** $p < 0.001$)

Fig. 5. Lung metastasis and extramedullary hematopoiesis with leuko-lymphocytosis. A) Metastasis quantification in lung by treatments group. Metastasis was significant decreased after the treatment with PGA-(G-AGM)-(Hyd-Dox)_{LL}, PGA-(G-AGM)-(EMCH-Dox)_{LL} and free Dox **B)** H&E Histological analysis of representative lung lobe receiving different treatments. Red arrowheads indicate metastatic nodules identified under the microscope. **C)** Tumor-induced splenomegaly, demonstrating maximum weight of spleen in control animals (PBS) and those treated with PGA-(G-AGM)-(Hyd-Dox)_{HL}. Spleens of mice treated with Dox, PGA-(G-AGM)-(Hyd-Dox)_{HL} or PGA-(G-AGM)-(Hyd-Dox)_{LL}, demonstrated significant spleen weight reduction. **D)** Histopathological examination of spleens of mice treated with different conjugates. Splenomegaly correlates with congested red pulp as demonstrated by H&E and CD-23 marker. 4T1 tumor development produced acute lymphocytosis and leukocytosis (with major proportion of segmented neutrophils) as seen in the PBS-treated mice (**E**, **F**, **G**). Animals treated with Dox and PGA-(G-AGM)-(Hyd-Dox)_{LL} demonstrated a recovery to the normal levels of lymphocytes and leukocytes. Statistical significance was determined using an ANOVA t-test (* $p < 0.05$, ** $p < 0.01$, *** $p < 0.001$ and **** $p < 0.0001$)

Fig. 6. Network visualization of the statistically significant GO terms grouped by hyper-categories. A) Venn diagram comparing the GO terms up or downregulated between PGA-(G-AGM)-(Hyd-Dox)_{LL}- PBS; PGA-(G-AGM)-(EMCH-Dox)_{LL} - PBS and PGA-(G-AGM)-(Hyd-Dox)_{LL}- PGA-(G-AGM)-(EMCH-Dox)_{LL} paired comparisons. Red numbers: upregulated GO terms; blue numbers: downregulated genes. Networks were constructed from these results and the more relevant are demonstrating similarities (**C**, **E**) and differences (**B**,

D) between the two drug conjugates. Networks constructed through REVIGO web server using EBI-GOA database. The darker the color the lower the p-value, as an indicative of significance level. Nodes size indicates the frequency of the GO term in the EBI-GOA database. Edges indicates highly similar GO terms regarding the number of genes shared. (PGA-(G-AGM)-(Hyd-Dox)_{LL} : **P-(Hyd)_{LL}**, PGA-(G-AGM)-(EMCH-Dox)_{LL} : **P-(EMCH)_{LL}**)

Fig. 7. Graphical model of the transcriptional responses to **PGA-(G-AGM)-(Hyd-Dox)_{LL}** and **PGA-(G-AGM)-(EMCH-Dox)_{LL}** conjugates. The model demonstrates the gene expression values measured by RNAseq of genes involved in **A)** Cell survival and apoptosis, and **B)** Inflammation, angiogenesis and metastasis. Each colored box depicts the log₂-fold change value between – from left to right – comparisons of PGA-(G-AGM)-(Hyd-Dox)_{LL} and PBS, PGA-(G-AGM)-(EMCH-Dox)_{LL} and PBS, and PGA-(G-AGM)-(Hyd-Dox)_{LL} and PGA-(G-AGM)-(EMCH-Dox)_{LL}. Blue indicates down-regulation and red up-regulation of gene expression, respectively, for each comparison. Green stars indicate statistically significant ($p < 0.01$) changes for each comparison; arrows indicate pathway relationships extracted from the KEGG pathway database: blunt ends indicate negative regulation and arrowheads indicate positive relationships.

FIGURES

FIG.1

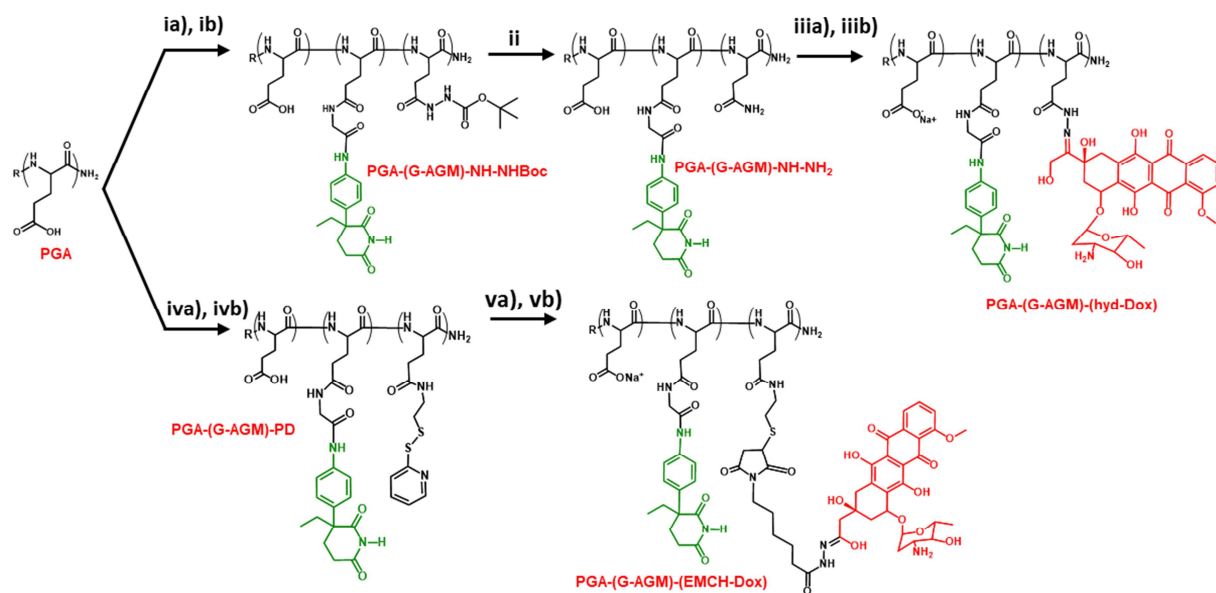


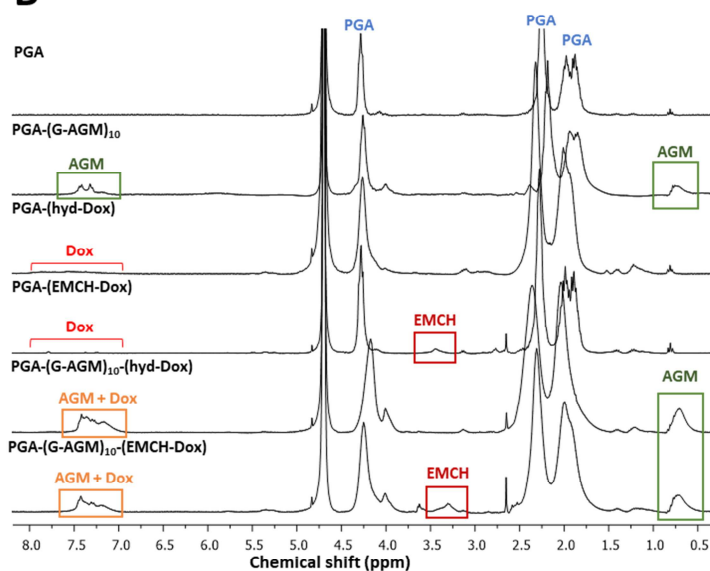
FIG.2

A

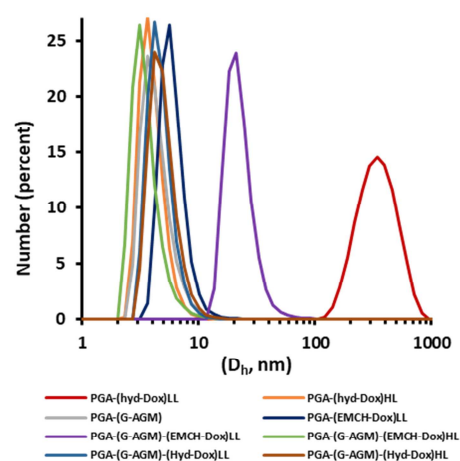
PGA conjugates	Dox Loading (mol%) ^A	AGM Loading (mol%) ^B	Size by DLS (D _h , nm) ^C	Theoretical Mw (kDa) ^D
PGA-(G-AGM) ₁₀	-	9.9	3.2	14830
PGA-(hyd-Dox) ₁	1.3	n/a	390.0	13090
PGA-(hyd-Dox) ₃	3.1	n/a	4.2	14100
PGA-(EMCH-Dox) ₁	0.8	n/a	6.5	12900
PGA-(G-AGM) ₁₀ -(hyd-Dox) ₁	1.1	9.1	4.4	14620
PGA-(G-AGM) ₁₀ -(hyd-Dox) ₃	2.9	10.4	3.6	14860
PGA-(G-AGM) ₁₀ -(EMCH-Dox) ₁	0.9	8.1	17.7	14900
PGA-(G-AGM) ₁₀ -(EMCH-Dox) ₃	2.9	9.4	3.2	15250

A: Calculated espectrophotometrically by UV-VIS; B: Averaged form ¹H-NMR and UV measurements; C: Size by Number; D: Calculated according to the drug loading

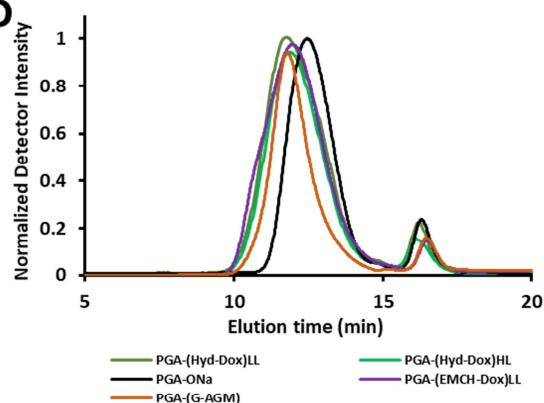
B



C



D



E

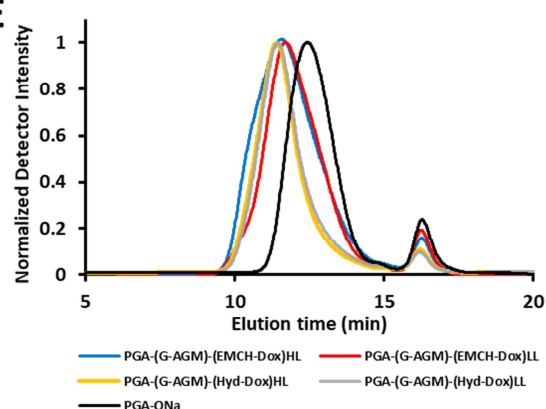


FIG.3

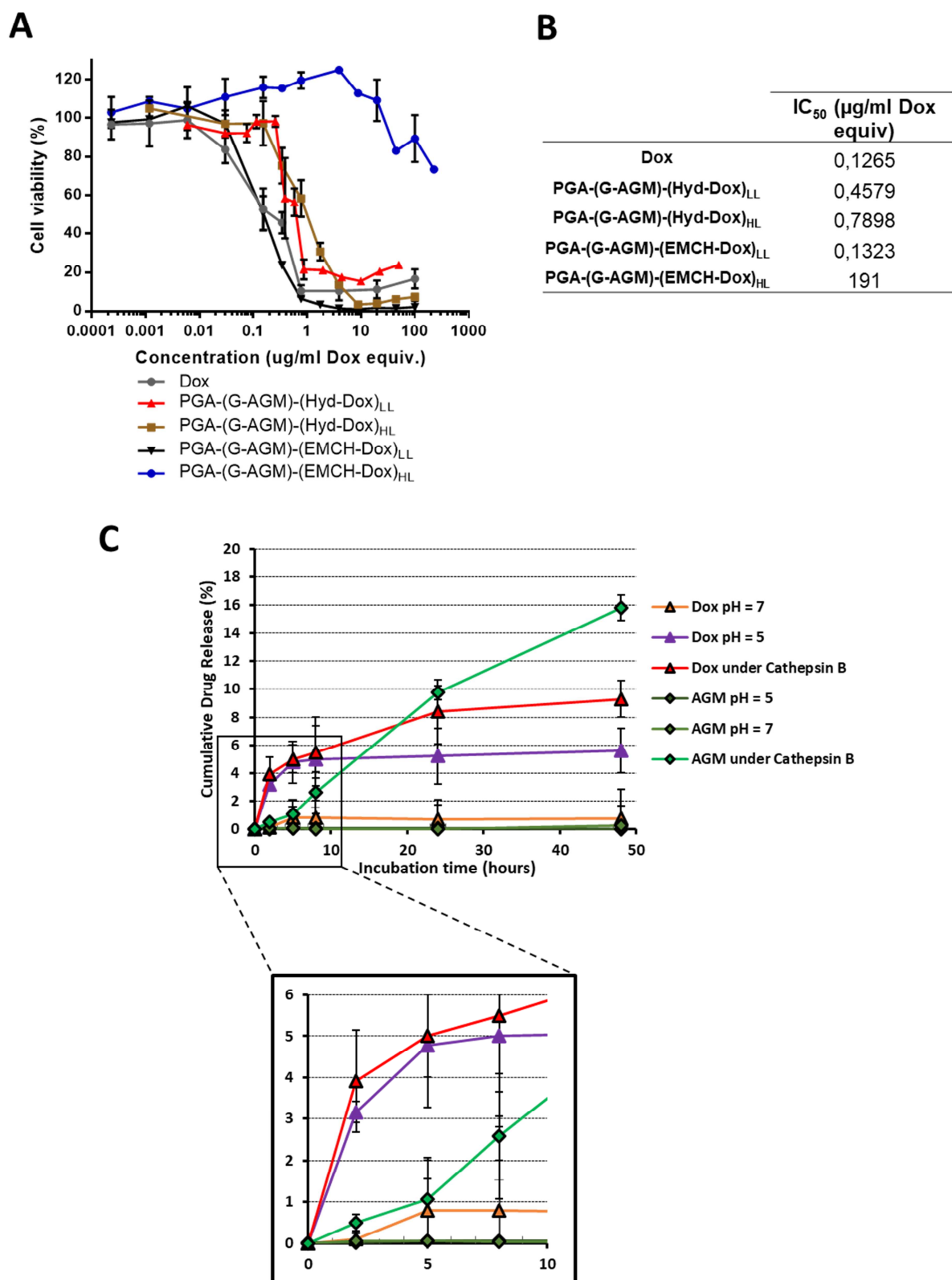


FIG.4

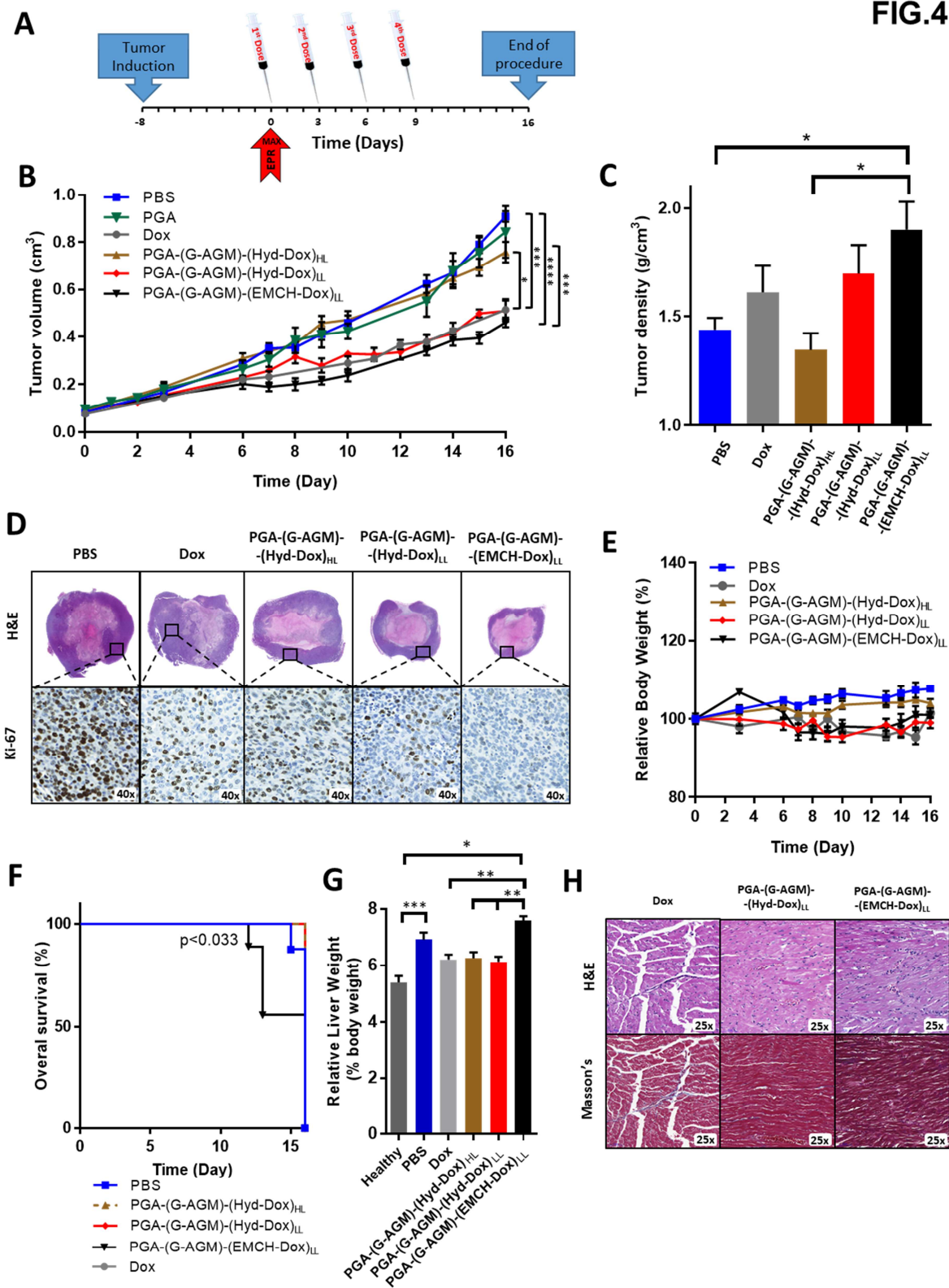


FIG.5

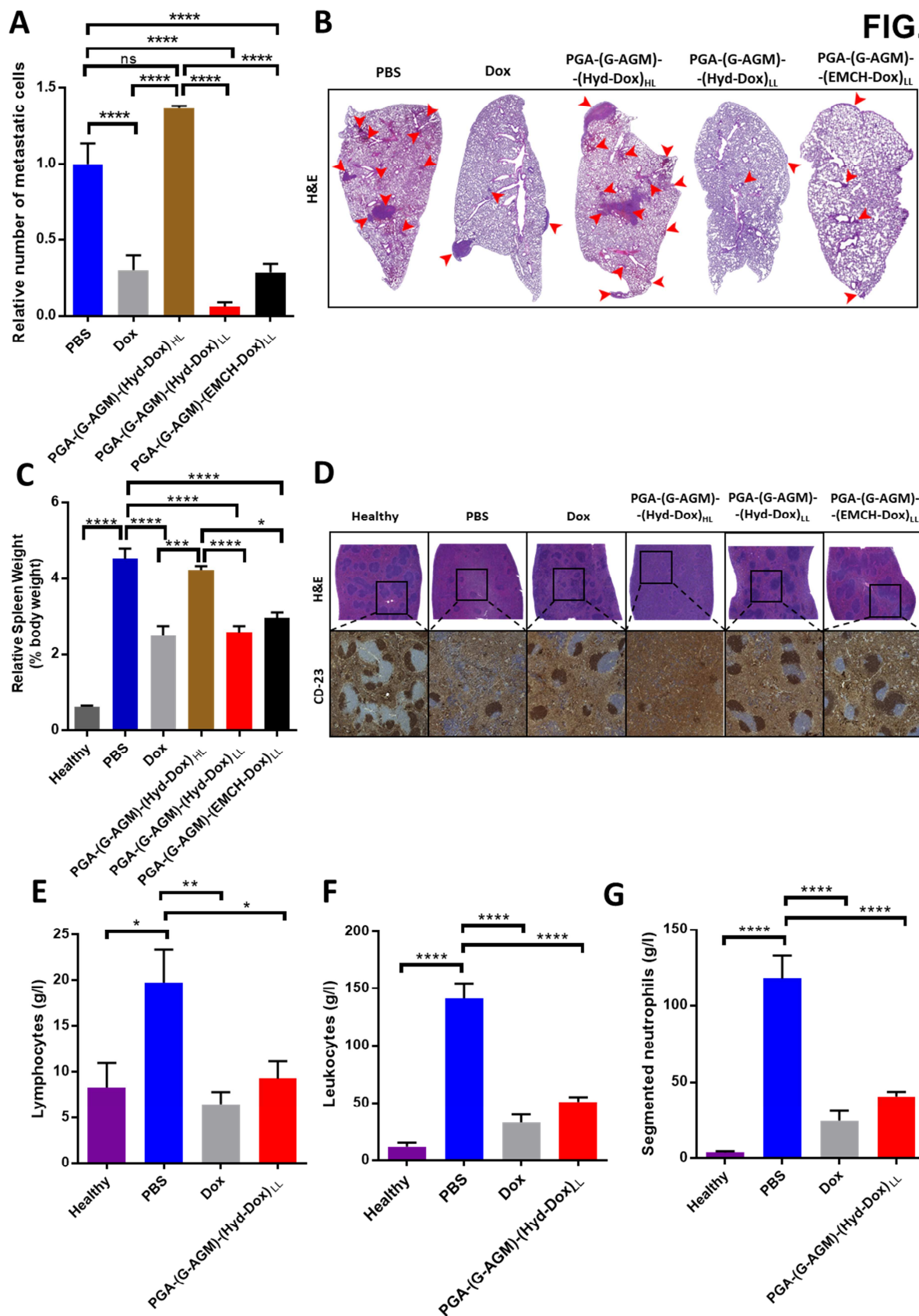
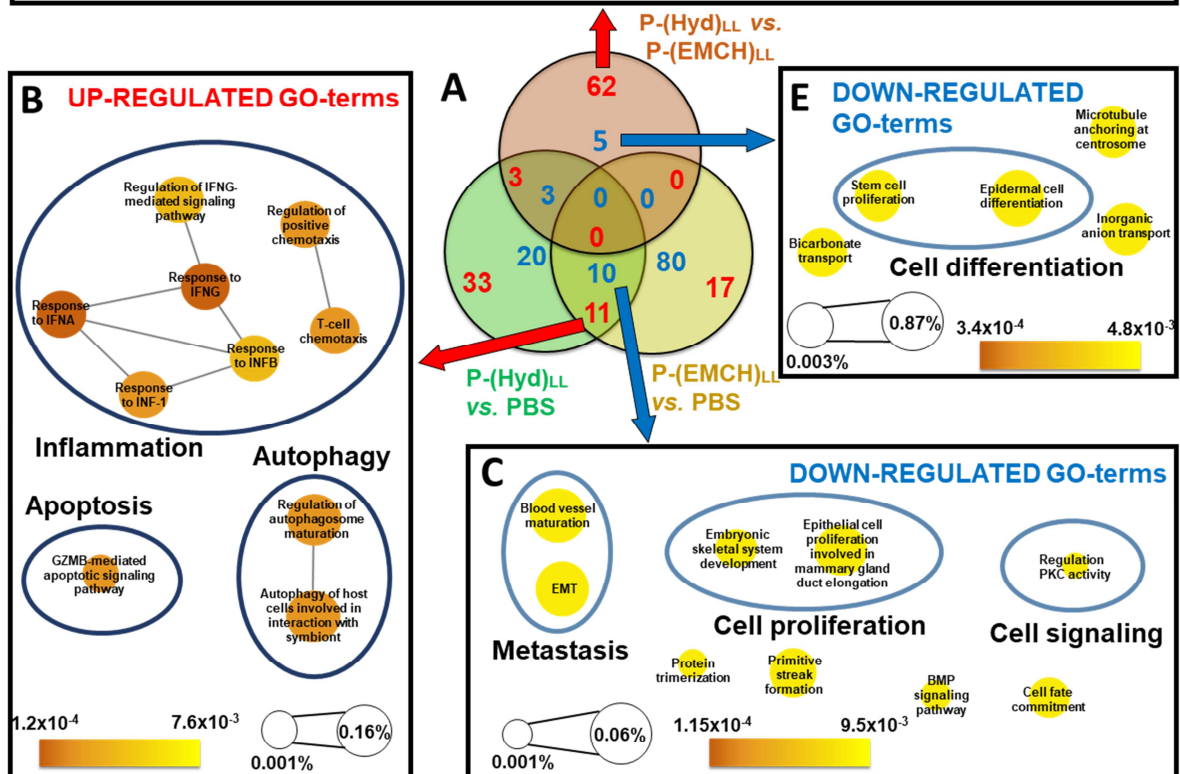
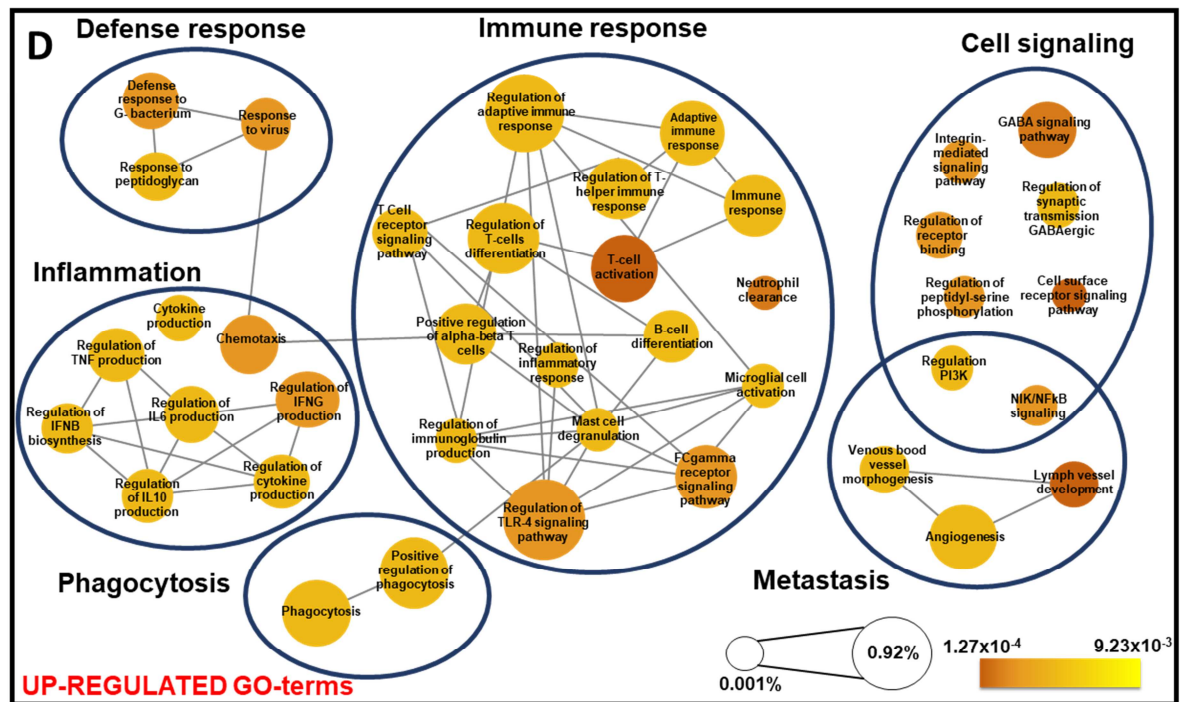
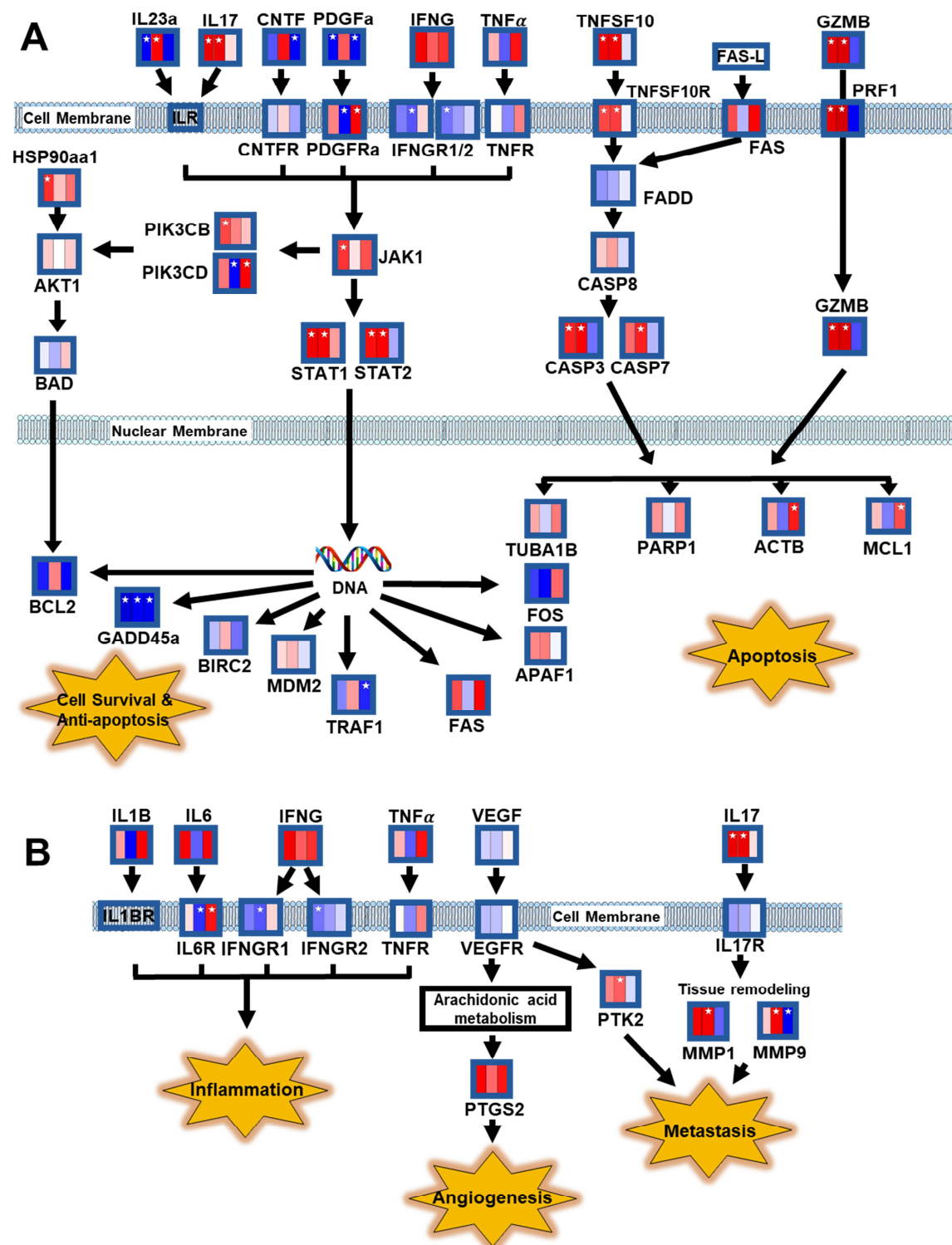


FIG.6



P-(Hyd)_{LL} = PGA-(G-AGM)-(Hyd-Dox)_{LL}
P-(EMCH)_{LL} = PGA-(G-AGM)-(EMCH-Dox)_{LL}
PBS = Placebo group (untreated mice)

FIG.7



Acknowledgements:

The authors would like to thank Dr. Stuart P. Atkinson for his collaboration in manuscript preparation and English revision, and Irene Borredá for essential immunohistological support. This work has been supported by the European Research Council (grant ERC-CoG-2014-648831 “MyNano”) and the Spanish Ministry of Science and Innovation (CTQ2010-18195, SAF2013-44848-R, BES-2008-006801, IPT-2012-0712-010000, Programa I3, and BIO2015-71658-R). LBN is funded through a University of South Florida-Helmsley Foundation award. FHL is funded through NIH grant. Part of the equipment employed in this work has been funded by Generalitat Valenciana and co-financed with FEDER funds (PO FEDER of Comunitat Valenciana 2014–2020).

Author Contributions:

- **Conception and design:** J.J.A-C., A.A., M.J.V.
- **Synthesis and characterization of the family of polymer-drug conjugates:** J.J.A-C
- ***In vivo* experiments optimization and development:** J.J.A-C., A.A., D.C.
- **Interpretation of histopathological data:** J. F., J.J.A-C., A.A.
- **Development of experimental methodology:** J.J.A-C., A.A., D.C., C.M.
- **Analysis and interpretation of data:** J.J.A-C., A.A., M.J.V., L.B-N., S.T., A.C.
- **Acquisition and interpretation of transcriptomic data:** L.B-N., S.T., A.A. J.J.A-C, M.J.V, A.C.
- **Writing, review, and/or revision of the manuscript:** J.J.A-C., A.A., M.J.V. L.B-N., A.C.
- **Study supervision:** A.A., M.J.V.

Data Availability Statement

The raw/processed data required to reproduce these findings cannot be shared at this time due to technical or time limitations. This data would be made available to the editor when ready.

References

- [1] Wang M, Zhao J, Zhang L, Wei F, Lian Y, Wu Y, et al. Role of tumor microenvironment in tumorigenesis. *J Cancer*. Sydney2017. p. 761-73.
- [2] Feng L, Ziliang D, Danlei T, Yicheng Z, Zhuang L. The acidic tumor microenvironment: a target for smart cancer nano-theranostics. *National Science Review*. 2018;5:269-86.
- [3] Maeda H. Tumor-Selective Delivery of Macromolecular Drugs via the EPR Effect: Background and Future Prospects. *Bioconjugate Chemistry*. 2010;21:797-802.
- [4] Maeda H, Tsukigawa K, Fang J. A Retrospective 30 Years After Discovery of the Enhanced Permeability and Retention Effect of Solid Tumors: Next-Generation Chemotherapeutics and Photodynamic Therapy--Problems, Solutions, and Prospects. *Microcirculation*. 2016;23:173-82.

- [5] Ojha T, Pathak V, Shi Y, Hennink WE, Moonen CTW, Storm G, et al. Pharmacological and physical vessel modulation strategies to improve EPR-mediated drug targeting to tumors. *Advanced drug delivery reviews*. 2017;119:44-60.
- [6] Kou L, Sun J, Zhai Y, He Z. The endocytosis and intracellular fate of nanomedicines: Implication for rational design. *Asian Journal of Pharmaceutical Sciences*. 2013;8:1-10.
- [7] Johnson DE, Ostrowski P, Jaumouillé V, Grinstein S. The position of lysosomes within the cell determines their luminal pH. *The Journal of Cell Biology*. 2016;212:677-92.
- [8] Arroyo-Crespo JJ, Deladriere C, Nebot VJ, Charbonnier D, Masiá E, Paul A, et al. Anticancer Activity Driven by Drug Linker Modification in a Polyglutamic Acid-Based Combination-Drug Conjugate. *Advanced Functional Materials*. 2018;28:1800931.
- [9] Paul A, Vicent MJ, Duncan R. Using Small-Angle Neutron Scattering to Study the Solution Conformation of N-(2-Hydroxypropyl)methacrylamide Copolymer–Doxorubicin Conjugates. *Biomacromolecules*. 2007;8:1573-9.
- [10] Arroyo-Crespo JJ, Armiñan A, Charbonnier D, Forteza J, Palomino-Schatzlein M, Pineda-Lucena A, et al. Triple-negative Breast Cancer Preclinical Models Provide Functional Evidence of Metastatic Progression and Suitability for Nanomedicine Evaluation Cancer Research. 2018;Under Review.
- [11] Zhong Y, Zhao J, Gu Yj, Zhao Y-f, Zhou Y-w, Fu G-X. Differential levels of cathepsin B and L in serum between young and aged healthy people and their association with matrix metalloproteinase 2. *Archives of Gerontology and Geriatrics*. 2015;61:285-8.
- [12] Atkinson S, Andreu Z, Vicent M. Polymer Therapeutics: Biomarkers and New Approaches for Personalized Cancer Treatment. *Journal of Personalized Medicine*. 2018;8:6.
- [13] Chipman SD, Oldham FB, Pezzoni G, Singer JW. Biological and clinical characterization of paclitaxel poliglumex (PPX, CT-2103), a macromolecular polymer-drug conjugate. *International journal of nanomedicine*. 2006;1:375-83.
- [14] Yu T, Di G. Role of tumor microenvironment in triple-negative breast cancer and its prognostic significance. *Chinese journal of cancer research = Chung-kuo yen cheng yen chiu*. 2017;29:237-52.
- [15] Xie HY, Shao ZM, Li DQ. Tumor microenvironment: driving forces and potential therapeutic targets for breast cancer metastasis. *Chinese journal of cancer*. 2017;36:36.
- [16] Kabanov AV. Polymer genomics: An insight into pharmacology and toxicology of nanomedicines. *Advanced Drug Delivery Reviews*. 2006;58:1597-621.
- [17] van Heeswijk WAR, Stoffer T, Eenink MJD, Potman W, van der Vijgh WJF, v.d. Poort J, et al. Synthesis, Characterization and Antitumor Activity of Macromolecular Prodrugs of Adriamycin. In: Anderson JM, Kim SW, editors. *Recent Advances in Drug Delivery Systems*. Boston, MA: Springer US; 1984. p. 77-100.
- [18] Willner D, Trail PA, Hofstead SJ, King HD, Lasch SJ, Braslawsky GR, et al. (6-Maleimidocaproyl)hydrazide of doxorubicin. A new derivative for the preparation of immunoconjugates of doxorubicin. *Bioconjugate Chemistry*. 1993;4:521-7.
- [19] Cai T, Chen Y, Wang Y, Wang H, Liu X, Jin Q, et al. Functional 2-methylene-1,3-dioxepane terpolymer: a versatile platform to construct biodegradable polymeric prodrugs for intracellular drug delivery. *Polymer Chemistry*. 2014;5:4061-8.
- [20] Pulaski BA, Ostrand-Rosenberg S. Mouse 4T1 breast tumor model. *Current protocols in immunology*. 2001;Chapter 20:Unit 20 2.
- [21] Dobin A, Davis CA, Schlesinger F, Drenkow J, Zaleski C, Jha S, et al. STAR: ultrafast universal RNA-seq aligner. *Bioinformatics*. 2013;29:15-21.
- [22] Li B, Dewey CN. RSEM: accurate transcript quantification from RNA-Seq data with or without a reference genome. *BMC Bioinformatics*. 2011;12:323.
- [23] Tarazona S, Furió-Tarí P, Turrà D, Pietro AD, Nueda MJ, Ferrer A, et al. Data quality aware analysis of differential expression in RNA-seq with NOISeq R/Bioc package. *Nucleic Acids Research*. 2015;43:e140-e.
- [24] Law CW, Chen Y, Shi W, Smyth GK. voom: precision weights unlock linear model analysis tools for RNA-seq read counts. *Genome Biology*. 2014;15:R29.

- [25] Smyth GK. Linear models and empirical bayes methods for assessing differential expression in microarray experiments. *Statistical applications in genetics and molecular biology*. 2004;3:Article3.
- [26] Benjamini Y, Hochberg Y. Controlling the False Discovery Rate: A Practical and Powerful Approach to Multiple Testing. *Journal of the Royal Statistical Society Series B (Methodological)*. 1995;57:289-300.
- [27] Hernandez-de-Diego R, Tarazona S, Martinez-Mira C, Balzano-Nogueira L, Furio-Tari P, Pappas GJ, Jr., et al. PaintOmics 3: a web resource for the pathway analysis and visualization of multi-omics data. *Nucleic acids research*. 2018.
- [28] Walker L, Perkins E, Kratz F, Raucher D. Cell penetrating peptides fused to a thermally targeted biopolymer drug carrier improve the delivery and antitumor efficacy of an acid-sensitive doxorubicin derivative. *International journal of pharmaceutics*. 2012;436:825-32.
- [29] Markovsky E, Baabur-Cohen H, Satchi-Fainaro R. Anticancer polymeric nanomedicine bearing synergistic drug combination is superior to a mixture of individually-conjugated drugs. *Journal of controlled release : official journal of the Controlled Release Society*. 2014;187:145-57.
- [30] Patterson JP, Robin MP, Chassenieux C, Colombani O, O'Reilly RK. The analysis of solution self-assembled polymeric nanomaterials. *Chemical Society Reviews*. 2014;43:2412-25.
- [31] Duro-Castano A, Nebot VJ, Nino-Pariente A, Arminan A, Arroyo-Crespo JJ, Paul A, et al. Capturing "Extraordinary" Soft-Assembled Charge-Like Polypeptides as a Strategy for Nanocarrier Design. *Advanced materials*. 2017;29.
- [32] Dionzou M, Morere A, Roux C, Lonetti B, Marty JD, Mingotaud C, et al. Comparison of methods for the fabrication and the characterization of polymer self-assemblies: what are the important parameters? *Soft matter*. 2016;12:2166-76.
- [33] Vicent MJ, Greco F, Nicholson RI, Paul A, Griffiths PC, Duncan R. Polymer therapeutics designed for a combination therapy of hormone-dependent cancer. *Angewandte Chemie*. 2005;44:4061-6.
- [34] DuPre SA, Redelman D, Hunter KW, Jr. The mouse mammary carcinoma 4T1: characterization of the cellular landscape of primary tumours and metastatic tumour foci. *International journal of experimental pathology*. 2007;88:351-60.
- [35] Arminan A, Palomino-Schatzlein M, Deladriere C, Arroyo-Crespo JJ, Vicente-Ruiz S, Vicent MJ, et al. Metabolomics facilitates the discrimination of the specific anti-cancer effects of free- and polymer-conjugated doxorubicin in breast cancer models. *Biomaterials*. 2018;162:144-53.
- [36] Lupertz R, Watjen W, Kahl R, Chovolou Y. Dose- and time-dependent effects of doxorubicin on cytotoxicity, cell cycle and apoptotic cell death in human colon cancer cells. *Toxicology*. 2010;271:115-21.
- [37] Bar-On O, Shapira M, Hershko DD. Differential effects of doxorubicin treatment on cell cycle arrest and Skp2 expression in breast cancer cells. *Anti-cancer drugs*. 2007;18:1113-21.
- [38] Peixoto RC, Miranda-Vilela AL, de Souza Filho J, Carneiro ML, Oliveira RG, da Silva MO, et al. Antitumor effect of free rhodium (II) citrate and rhodium (II) citrate-loaded maghemite nanoparticles on mice bearing breast cancer: a systemic toxicity assay. *Tumour biology : the journal of the International Society for Oncodevelopmental Biology and Medicine*. 2015;36:3325-36.
- [39] Zhou M, Ku G, Paeon L, Li C. Theranostic probe for simultaneous in vivo photoacoustic imaging and confined photothermolysis by pulsed laser at 1064 nm in 4T1 breast cancer model. *Nanoscale*. 2014;6:15228-35.
- [40] Caruso RA, Branca G, Fedele F, Irato E, Finocchiaro G, Parisi A, et al. Mechanisms of coagulative necrosis in malignant epithelial tumors (Review). *Oncology letters*. 2014;8:1397-402.
- [41] Chawla SP, Cranmer LD, Tine BAV, Reed DR, Okuno SH, Butrynski JE, et al. Phase II Study of the Safety and Antitumor Activity of the Hypoxia-Activated Prodrug TH-302 in Combination With Doxorubicin in Patients With Advanced Soft Tissue Sarcoma. *Journal of Clinical Oncology*. 2014;32:3299-306.
- [42] Shivakumar P, Rani MU, Reddy AG, Anjaneyulu Y. A study on the toxic effects of Doxorubicin on the histology of certain organs. *Toxicology international*. 2012;19:241-4.

- [43] Tacar O, Sriamornsak P, Dass CR. Doxorubicin: an update on anticancer molecular action, toxicity and novel drug delivery systems. *The Journal of pharmacy and pharmacology*. 2013;65:157-70.
- [44] Alves AC, Magarkar A, Horta M, Lima J, Bunker A, Nunes C, et al. Influence of doxorubicin on model cell membrane properties: insights from in vitro and in silico studies. *Scientific reports*. 2017;7:6343.
- [45] Thorn CF, Oshiro C, Marsh S, Hernandez-Boussard T, McLeod H, Klein TE, et al. Doxorubicin pathways: pharmacodynamics and adverse effects. *Pharmacogenetics and genomics*. 2011;21:440-6.
- [46] Hrelia S, Fiorentini D, Maraldi T, Angeloni C, Bordoni A, Biagi PL, et al. Doxorubicin induces early lipid peroxidation associated with changes in glucose transport in cultured cardiomyocytes. *Biochimica et biophysica acta*. 2002;1567:150-6.
- [47] Gao D, Du J, Cong L, Liu Q. Risk Factors for Initial Lung Metastasis from Breast Invasive Ductal Carcinoma in Stages I–III of Operable Patients. *Japanese Journal of Clinical Oncology*. 2009;39:97-104.
- [48] Liu M, Jin X, He X, Pan L, Zhang X, Zhao Y. Macrophages support splenic erythropoiesis in 4T1 tumor-bearing mice. *PloS one*. 2015;10:e0121921.
- [49] DuPre SA, Hunter KW, Jr. Murine mammary carcinoma 4T1 induces a leukemoid reaction with splenomegaly: association with tumor-derived growth factors. *Experimental and molecular pathology*. 2007;82:12-24.
- [50] Perry JL, Reuter KG, Luft JC, Pecot CV, Zamboni W, DeSimone JM. Mediating Passive Tumor Accumulation through Particle Size, Tumor Type, and Location. *Nano letters*. 2017;17:2879-86.
- [51] Platanias LC. Mechanisms of type-I- and type-II-interferon-mediated signalling. *Nature reviews Immunology*. 2005;5:375-86.
- [52] de Weerd NA, Samarajiwa SA, Hertzog PJ. Type I interferon receptors: biochemistry and biological functions. *The Journal of biological chemistry*. 2007;282:20053-7.
- [53] Arellano G, Ottum PA, Reyes LI, Burgos PI, Naves R. Stage-Specific Role of Interferon-Gamma in Experimental Autoimmune Encephalomyelitis and Multiple Sclerosis. *Frontiers in immunology*. 2015;6:492.
- [54] Elmore S. Apoptosis: a review of programmed cell death. *Toxicologic pathology*. 2007;35:495-516.
- [55] Yin Z, Pascual C, Klionsky DJ. Autophagy: machinery and regulation. *Microbial cell*. 2016;3:588-96.
- [56] Slaney CY, Kershaw MH, Darcy PK. Trafficking of T Cells into Tumors. *Cancer Research*. 2014;74:7168-74.
- [57] Ribatti D. Epithelial-mesenchymal transition in morphogenesis, cancer progression and angiogenesis. *Experimental cell research*. 2017;353:1-5.
- [58] Sanchez-Garcia I. The crossroads of oncogenesis and metastasis. *The New England journal of medicine*. 2009;360:297-9.
- [59] Holderfield MT, Hughes CCW. Crosstalk Between Vascular Endothelial Growth Factor, Notch, and Transforming Growth Factor- β in Vascular Morphogenesis. *Circulation Research*. 2008;102:637-52.
- [60] Montévil M, Speroni L, Sonnenschein C, Soto AM. Modeling mammary organogenesis from biological first principles: Cells and their physical constraints. *Progress in Biophysics and Molecular Biology*. 2016;122:58-69.
- [61] Lanigan F, O'Connor D, Martin F, Gallagher WM. Common Molecular Mechanisms of Mammary Gland Development and Breast Cancer. *Cellular and Molecular Life Sciences*. 2007;64:3159-84.
- [62] Garg A, Aggarwal BB. Nuclear transcription factor-kappaB as a target for cancer drug development. *Leukemia*. 2002;16:1053-68.
- [63] Strasser A, O'Connor L, Dixit VM. Apoptosis signaling. *Annual review of biochemistry*. 2000;69:217-45.
- [64] Balzano L, Diez N. Mecanismos asociados a la agresividad tumoral y su empleo para diagnosticar este fenómeno. *RET Revista de Estudios Transdisciplinarios*. 2010;2:77-86.